Journal of Computational Physics 336 (2017) 261–274

Contents lists available at ScienceDirect

Journal of Computational Physics

www.elsevier.com/locate/jcp

Iterative Brinkman penalization for simulation of impulsively started flow past a sphere and a circular disc

Henrik Juul Spietz [a], Mads Mølholm Hejlesen [a], Jens Honoré Walther [a,b,*]

[a] Department of Mechanical Engineering, Technical University of Denmark, Building 403, DK-2800 Kgs. Lyngby, Denmark
[b] Computational Science and Engineering Laboratory, ETH Zürich, Clasiusstrasse 33, CH-8092 Zürich, Switzerland

ARTICLE INFO

Article history:
Received 12 August 2016
Received in revised form 24 January 2017
Accepted 27 January 2017
Available online 2 March 2017

Keywords:
Vortex method
Brinkman penalization
3D flow
Sphere
Disc

ABSTRACT

We present a Brinkman penalization method for three-dimensional (3D) flows using particle vortex methods, improving the existing technique by means of an iterative process. We perform simulations to study the impulsively started flow past a sphere at $Re = 1000$ and normal to a circular disc at $Re = 500$. The simulation results obtained for the flow past a sphere are found in qualitative good agreement with previously published results obtained using respectively a 3D vortex penalization method and a 3D vortex method combined with an accurate boundary element method. From the results obtained for the flow normal to a circular disc it is found that the iterative method enables the use of a time step that is one order of magnitude larger than required by the standard non-iterative Brinkman penalization method.

© 2017 Elsevier Inc. All rights reserved.

1. Introduction

Conventionally, the analysis of fluid-structure interaction requires the use of body-fitted grids to enforce the no-slip boundary condition on computational points located at the solid-fluid interface. The solid boundary condition may also be enforced with uniform grids using immersed boundary methods [1,2] or fictitious domain methods which rely on a modification of the governing equations. These methods may be interesting since they avoid time consuming generation of high quality, non-orthogonal grids, that require non-trivial solution algorithms.

One immersed boundary method is the Brinkman penalization method [3–5]. The principle of the method is to model a fluid flow in a porous medium by adding volume forcing to the governing equations. The porous medium flow tends to the primary flow past a non-porous immersed body as the permeability is reduced to zero in the part of the flow occupied by the solid body.

In the field of vortex methods several numerical schemes are based on this method [6–13]. Hejlesen et al. [7] proposed an iterative variation of the explicit scheme for the simulation of two-dimensional (2D) fluid flow past solid obstacles with the Vortex–In–Cell (VIC) algorithm. This iterative method uses a split-step scheme that overcomes a drawback of the conventional non-iterative schemes for vorticity-velocity formulation of the Navier–Stokes equations. For the non-iterative schemes an accurate enforcement of the solid boundary condition restricts the time step size because the numerical formulation lacks the global coupling of the elliptic kinematic equation. In this paper we show that the method is extendable to 3D flows. The proposed method is applied to the impulsively started flow past a sphere and the results are compared to results

* Corresponding author at: Department of Mechanical Engineering, Technical University of Denmark, Building 403, DK-2800 Kgs. Lyngby, Denmark. Fax: + 45 4588 4325.
E-mail address: jhw@mek.dtu.dk (J.H. Walther).

http://dx.doi.org/10.1016/j.jcp.2017.01.064
0021-9991/© 2017 Elsevier Inc. All rights reserved.

by Mimeau et al. [13] and Ploumhans et al. [14]. The work by Mimeau et al. [13] includes a study of the flow past a sphere using the non-iterative implicit penalization. The focus of their studies is on the space-developing simulations since the velocity-vorticity relation is solved using a periodic Poisson solver with a velocity correction step to account for outflow of vorticity in the stream wise direction. Results are obtained for $\mathrm{Re} = 300$ and $\mathrm{Re} = 1000$ in simulated times long enough for the flows to reach a steady state. In the present study, we focus on the impact of an iterative process on accelerated flows, hence our approach avoids potential artifacts due to outflow boundary conditions. However, this limits the time span of the simulation due to growing extent of domain with time. Similarly Ploumhans et al. [14] studied this flow at various Reynolds numbers using a particle vortex method combined with a boundary element method (BEM) and panel-vortex diffusion to enforce the no-slip condition at the fluid-solid interface. They did not use outflow boundary conditions, but a mapping to a non-uniform grid to reduce the computational costs. Moreover, we present results for the simulation of the impulsively started flow normal to a circular disc of finite thickness at $\mathrm{Re} = 500$.

2. Methodology

2.1. The Brinkman penalization method

We solve the incompressible Navier–Stokes equations in a domain (Ω) consisting of a solid region ($\mathcal{S} \in \Omega$) and a fluid region ($\mathcal{F} = \Omega \setminus \mathcal{S}$). We introduce the Brinkman term that penalizes the difference between the solid velocity ($\boldsymbol{u}_s$) and the fluid velocity ($\boldsymbol{u}$) within the solid body to be close to zero [3]. Here we consider the vorticity-velocity formulation of the Navier–Stokes equations

$$\frac{\partial \boldsymbol{\omega}}{\partial t} + (\boldsymbol{u} \cdot \nabla)\boldsymbol{\omega} = (\boldsymbol{\omega} \cdot \nabla)\boldsymbol{u} + \nu \nabla^2 \boldsymbol{\omega} + \nabla \times [\lambda \chi (\boldsymbol{u}_s - \boldsymbol{u})], \tag{1}$$

where ν is the kinematic viscosity of the fluid and λ is a penalization parameter, which may be seen as the inverse permeability of the solid region. χ is the characteristic function of $\mathcal{S}$

$$\chi(\boldsymbol{x}) = \begin{cases} 1 & \text{for } \boldsymbol{x} \in \mathcal{S} \\ 0 & \text{for } \boldsymbol{x} \in \mathcal{F}. \end{cases} \tag{2}$$

We derive the kinematic relation between the dependent variables by applying a Helmholtz decomposition for the velocity ($\boldsymbol{u}$) by requiring the vector potential ($\boldsymbol{\psi}$) to be solenoidal

$$\boldsymbol{u} = \nabla \times \boldsymbol{\psi} - \nabla \phi, \quad \nabla \cdot \boldsymbol{\psi} = 0 \tag{3}$$

The vorticity may then be related to the velocity by a Poisson equation through the vector potential or the velocity directly

$$\nabla^2 \boldsymbol{\psi} = -\boldsymbol{\omega}, \tag{4}$$

$$\nabla^2 \boldsymbol{u} = -\nabla \times \boldsymbol{\omega}. \tag{5}$$

We note that the Brinkman penalization term may be expanded as

$$\nabla \times [\lambda \chi (\boldsymbol{u}_s - \boldsymbol{u})] = \lambda \nabla \chi \times (\boldsymbol{u}_s - \boldsymbol{u}) + \lambda \chi (\boldsymbol{\omega}_s - \boldsymbol{\omega}), \tag{6}$$

where $\boldsymbol{\omega}_s = \nabla \times \boldsymbol{u}_s$. The term causes a production of vorticity in Eq. (1) due to residual in the velocity field ($\boldsymbol{u}_s - \boldsymbol{u}$) and vorticity field ($\boldsymbol{\omega}_s - \boldsymbol{\omega}$). $\nabla \chi$ is a vector field with non-zero magnitude only at the fluid-solid interface and is orientated normal to the interface. Hence, this production term is zero where the residual velocity ($\boldsymbol{u}_s - \boldsymbol{u}$) is also normal to the interface. As a consequence, when the Brinkman term is approximated separately from the elliptic kinematic relation between the dependent variables, the enforcement of the solid boundary condition will be delayed in time. This short-coming is distinctive in accelerated flows past objects, whose geometries have the majority of the surface area normal to the flow direction. This effect has been illustrated by Hejlesen et al. [7] for the impulsively started flow normal to a flat plate and it is the motivation for considering the impulsively started flow normal to a circular disc in the present study.

2.2. Numerical implementation of the Brinkman penalization method in a re-meshed vortex method

We solve the modified vorticity transport equation (Eq. (1)) in a split-step algorithm

$$\frac{\partial \boldsymbol{\omega}}{\partial t} = \nabla \times [\lambda \chi (\boldsymbol{u}_s - \boldsymbol{u})], \tag{7}$$

$$\frac{D\boldsymbol{\omega}}{Dt} = (\boldsymbol{\omega} \cdot \nabla)\boldsymbol{u} + \nu \nabla^2 \boldsymbol{\omega}. \tag{8}$$

Our principle for solving Eq. (8) is to use the VIC method, where $\boldsymbol{\omega}$ is discretized onto N_p discrete particles carrying vorticity ($\boldsymbol{\omega}_p$). The particle vorticity is interpolated to a uniform grid of spacing h using a third order accurate interpolation kernel (M_4') [15] as

$$\boldsymbol{\omega}(\boldsymbol{x},t)=\sum_{p}^{N_p}\boldsymbol{\omega}_p W\left(\frac{\boldsymbol{x}-\boldsymbol{x}_p}{h}\right),\quad W(\boldsymbol{x})=M_4'(x)M_4'(y)M_4'(z), \tag{9}$$

$$M_4'(x)=\begin{cases}0 & \text{for } |x|>2\\ \frac{1}{2}(2-|x|)^2(1-|x|) & \text{for } 1<|x|\le 2\\ 1-\frac{5|x|^2}{2}+\frac{3|x|^3}{2} & \text{for } |x|\le 1.\end{cases} \tag{10}$$

Another kernel used for interpolation in vortex methods of fourth order accuracy (M_6^*) introduced in [16] has been shown to significantly improve the accuracy of the 3D vortex method in marginally resolved and underresolved simulations [17]. The stencil of the discrete interpolation operator based on M_4' consists of 64 grid points whereas it consists of 216 grid points if based on M_6^*. Hence interpolation and re-meshing is computationally more expensive using M_6^* as compared to M_4' since the cost is proportional to the stencil size.

Using the discrete approximation, Eq. (8) becomes a system of coupled ordinary differential equations, which is solved in the Lagrangian frame of reference

$$\frac{\mathrm{d}\boldsymbol{x}_p}{\mathrm{d}t}=\boldsymbol{u}(\boldsymbol{x}_p,t) \tag{11}$$

$$\frac{\mathrm{d}\boldsymbol{\omega}_p}{\mathrm{d}t}=\left[(\boldsymbol{\omega}\cdot\nabla)\boldsymbol{u}+\nu\nabla^2\boldsymbol{\omega}\right]_p. \tag{12}$$

On the grid, the Poisson equation (Eq. (4)) is solved as a convolution with a tenth order accurate regularized free-space Green's function solution ($G_\epsilon(\boldsymbol{x})$) as

$$\boldsymbol{\psi}(\boldsymbol{x})=\int_{-\infty}^{\infty}G_\epsilon(\boldsymbol{x}'-\boldsymbol{x})\boldsymbol{\omega}(\boldsymbol{x})\,\mathrm{d}\boldsymbol{x}'=G_\epsilon*\boldsymbol{\omega}, \tag{13}$$

where $*$ denotes convolution. For details on the regularized Green's function the reader is referred to [18–20]. To calculate the convolution we use the Fast Fourier Transform (FFT) and the zero-padding technique to impose free-space conditions as proposed by Hockney and Eastwood [21–23]. The velocity is recovered from $\boldsymbol{\psi}$ by Eq. (3) where we consider a uniform free-stream with velocity $\boldsymbol{U}$ as the only irrotational contribution

$$\boldsymbol{u}=\nabla\times\boldsymbol{\psi}+\boldsymbol{U}. \tag{14}$$

Stretching and diffusion of vorticity in Eq. (12) are approximated using fourth order accurate centered finite difference operators on the mesh. The right-hand-sides of Eq. (11) and Eq. (12) are evaluated at particle positions by interpolation from mesh fields to advance the particles in an explicit Runge–Kutta time stepping scheme. To ensure the consistency of the method [24,25], the particles are uniformly re-sampled from the mesh field (re-meshed) once every time step.

The convective transport term ($(\boldsymbol{u}\cdot\nabla)\boldsymbol{\omega}$) does not explicitly appear in the Lagrangian formulation Eq. (11) and Eq. (12), hence the time step used with the method is not limited by the usual CFL condition. Instead, the time step is limited by a strain time scale [26]

$$\|\omega\|_\infty\Delta t<\mathcal{O}(1). \tag{15}$$

In addition, the spatiotemporal discretization of the solution yields a Fourier condition due to the viscous term as in Eulerian methods

$$\frac{\nu\Delta t}{h^2}<C. \tag{16}$$

The constant (C) depends on the time stepping scheme. For the explicit Runge–Kutta schemes considered $C=\frac{1}{4}$.

We denote the solution to Eq. (7) $\boldsymbol{\omega}^*$ and the corresponding velocity field $\boldsymbol{u}^*$. We write the solution as a correction to the vorticity field ($\boldsymbol{\xi}$) prior to this step ($\boldsymbol{\omega}$)

$$\boldsymbol{\omega}^*=\boldsymbol{\omega}+\boldsymbol{\xi}. \tag{17}$$

The correction may be determined by discretizing Eq. (7) using either the explicit or the implicit Euler scheme as respectively

$$\boldsymbol{\xi}^*_{\mathrm{exp}}=\nabla\times[\Delta t\lambda\chi(\boldsymbol{u}_s-\boldsymbol{u})] \tag{18}$$

or

$$\boldsymbol{\xi}^*_{\mathrm{imp}}=\nabla\times\left[\Delta t\lambda\chi(\boldsymbol{u}_s-\boldsymbol{u}^*)\right]=\nabla\times\left[\frac{\Delta t\lambda\chi}{1+\Delta t\lambda\chi}(\boldsymbol{u}_s-\boldsymbol{u})\right]. \tag{19}$$

In the Brinkman method λ is controlling how effectively the solid boundary condition is enforced, hence it is desirable to set it as large possible. The explicit scheme (Eq. (18)) is stable for $0 < \lambda \leq \frac{2}{\Delta t}$ whereas the implicit scheme (Eq. (19)) is unconditionally stable and thus formally better suited for the discretization. However, Rasmussen et al. [27] noticed that when the explicit scheme is used with $\lambda = \frac{1}{\Delta t}$ the two schemes are essentially the same and differs only in the way the mollified characteristic function of the solid blends into the fluid. We note that

$$\lim_{\lambda=\infty} \frac{\Delta t \lambda \chi}{1 + \Delta t \lambda \chi} = \chi. \tag{20}$$

Consequently, if the mask (χ) is a Heaviside function the implicit scheme, in the limit of $\lambda \to \infty$, is equivalent to the explicit scheme using $\lambda = \frac{1}{\Delta t}$.

When the Brinkman method is used in a discrete vorticity formulation as Eq. (18) or Eq. (19), the grid points where penalization vorticity ($\boldsymbol{\xi}$) may be produced in a single time step will depend on velocity residual within the solid ($\boldsymbol{u}_s - \boldsymbol{u}^n$) and on the geometry of the solid cf. Eq. (6). Hence, only if the penalization vorticity is found, while invoking the elliptic relation between vorticity and velocity cf. Eq. (5), a strong coupling between the two dependent variables may be enforced in the general case. To achieve this we compute the split-step result ($\boldsymbol{\omega}^*$) in a number of iterations (N_i) as Eq. (21) and Eq. (22) using an update based on a generalization of Eq. (18).

$$\boldsymbol{\xi}^{k+1} = \boldsymbol{\xi}^k + \alpha \nabla \times \left[\chi \left(\boldsymbol{u}_s - (\boldsymbol{u} + \boldsymbol{u}_\xi^k) \right) \right], \tag{21}$$

$$\nabla^2 \boldsymbol{u}_\xi^{k+1} = -\nabla \times \boldsymbol{\xi}^{k+1} \quad \text{for} \quad k = 1, 2, \ldots N_i. \tag{22}$$

Here α is a relaxation parameter, and the process is stable for $0 < \alpha \leq 2$. The reader is referred to Hejlesen et al. [7] for the details on the derivation of Eq. (21) and Eq. (22).

Termination of the process we base on a criteria using the second norm of vorticity ($\mathcal{E}$) introduced between iterations as

$$\frac{|\mathcal{E}^{k+1} - \mathcal{E}^k|}{\mathcal{E}^k} < \varepsilon, \quad \mathcal{E}^k = \int \boldsymbol{\xi}^k \cdot \boldsymbol{\xi}^k \, \mathrm{d}V, \tag{23}$$

where ε is a specified tolerance.

The accuracy of the Brinkman method may be quantified by considering the residual velocity ($||\frac{\boldsymbol{u}_s - \boldsymbol{u}}{U}||$) within the solid. When the Brinkman method is used in the velocity-pressure formulation the L_∞-norm of the residual velocity has been related to λ as $\mathcal{O}\left(\lambda^{-0.5}\right)$ by Angot et al. [3].

This relationship does not hold in the general case as the geometry of the solid may have a significant influence as shown by Hejlesen et al. [7], who considered the vorticity formulation.

In the iterative process (Eq. (21) and Eq. (22)) λ has been eliminated as a free parameter and replaced it by a relaxation parameter (α) and a termination criteria governing the number of iterations (N_i). We observe from experiments that using the iterative process the residual is reduced with the iteration number asymptotically as $\mathcal{O}\left(N_i^n\right)$, where $n \simeq -0.5$ independent of the global time step.

In the present method $\boldsymbol{\xi}$ will be non-zero only in the immediate vicinity of the solid body if a compact approximation to the curl in Eq. (21) is applied. In flows where the solid region is small compared to extend of the vorticity field, the computational efforts associated with solving the Poisson equation for $\boldsymbol{u}_\xi$ every iteration is reduced by computing $\boldsymbol{\xi}$ separately from $\boldsymbol{\omega}$ using a smaller sub-set of the computational grid.

Other implementations of the Brinkman penalization method [10,6,8] have replaced χ by a smooth approximation, since it is a Heaviside function, and the derivative of a Heaviside function is a singularity. In the present study we approximate the curl of the term $\chi(\boldsymbol{u}_s - \boldsymbol{u})$ (that may be discontinuous) by second order finite difference (unless otherwise specified) to avoid the dependency on an additional mollification length. The higher order, regularized Poisson solver guarantees a smooth velocity field and in addition, the penalized vorticity field is smoothed explicitly to be consistent with the regularized solution obtained with the higher order Poisson solver. This we do by linear convolution of the vorticity field with a regularization kernel (ζ_ϵ)

$$\boldsymbol{\omega}_\epsilon = \zeta_\epsilon * \boldsymbol{\omega}. \tag{24}$$

We use a tenth order accurate regularization kernel in Eq. (24) consistent with Eq. (13). For the details of the derivation of ζ_ϵ the reader is referred to [18–20].

For additional details on the implementation of the iterative penalization in the re-meshed vortex method and for an outline of the algorithm the reader is referred to Hejlesen et al. [7].

In the VIC method the velocity field is computed from the vorticity field. To avoid an accumulation of divergence errors the intermediate vorticity field ($\tilde{\boldsymbol{\omega}}$) is re-projected onto a divergence-free field ($\boldsymbol{\omega} = \nabla \times \boldsymbol{u}$) once every time step while applying the smoothing (24). This we do by applying a Helmholtz decomposition to the vorticity field

$$\tilde{\boldsymbol{\omega}} = \nabla \times \boldsymbol{u} - \nabla a, \quad \nabla \cdot \boldsymbol{u} = 0. \tag{25}$$

Hence, we solve the Poisson equation (Eq. (26)) for the scalar potential (a) and add ∇a to the filtered vorticity field

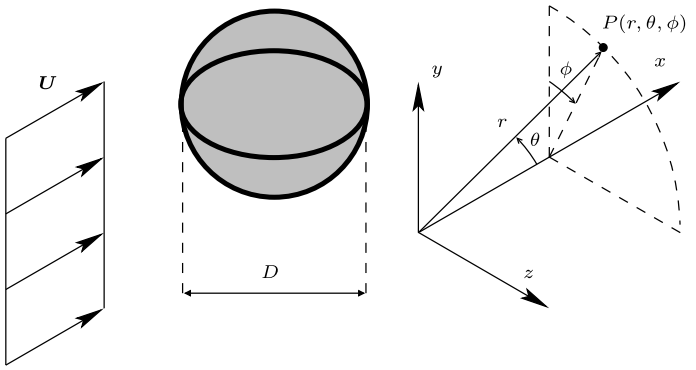

Fig. 1. Impulsively started flow ($\boldsymbol{U}$) past a sphere of diameter (D). A Cartesian coordinate system (x, y, z) and a spherical coordinate system (r, θ, ϕ) have also been indicated. The origin of the coordinate systems is in the sketch displaced from their actual origin being the center of the sphere.

$$\nabla^2 a = -\nabla \cdot \tilde{\boldsymbol{\omega}} \tag{26}$$

$$\boldsymbol{\omega} = \tilde{\boldsymbol{\omega}} + \nabla a. \tag{27}$$

It is noted that the smoothing (Eq. (24)) introduces additional diffusion to the full vorticity field, but that the re-projection (Eq. (27)) in itself does not modify the vorticity field if the divergence is zero.

2.3. Calculation of the aerodynamic force

The total aerodynamic force acting on a solid body may be computed from the rate of change of the first order moment of the vorticity distribution and an inertia term cf. Wu [28]. For a rigid body moving with solid body velocity ($\tilde{\boldsymbol{u}}_s$) the force is given by

$$\boldsymbol{F} = -\rho \frac{1}{2} \frac{\mathrm{d}}{\mathrm{d}t} \int_{\Omega} \boldsymbol{x} \times \boldsymbol{\omega} \, \mathrm{d}V + \rho \frac{\mathrm{d}}{\mathrm{d}t} \int_{\mathcal{S}} \tilde{\boldsymbol{u}}_s \, \mathrm{d}V, \tag{28}$$

where ρ is the density of the fluid. We note, that Eq. (28) requires and integration over the entire vorticity field extending e.g., to the far wake of the flow. Ploumhans et al. [14] noted, that this global formulation may be inaccurate when having a coarse spatial resolution in the far wake and found the local control volume approach by Noca et al. [29,30] to be more accurate. In the present work it has been noticed that the global approach is also sensitive to truncation, introduced when the vorticity is advected out of the computational domain, that in practice is necessary to limit the computational effort in space-developing simulations. Instead we utilize that a change in the first moment of vorticity may only be due to non-conservative external forcing in the momentum equation [31], which in the present study is due to the penalization function. Following Hejlesen et al. [7] we therefore exploit the vorticity decomposition Eq. (17) in Eq. (28) to obtain

$$\boldsymbol{F} = -\rho \frac{1}{2} \frac{\mathrm{d}}{\mathrm{d}t} \int_{\Omega} \boldsymbol{x} \times \boldsymbol{\xi} \, \mathrm{d}V + \rho \frac{\mathrm{d}}{\mathrm{d}t} \int_{\mathcal{S}} \tilde{\boldsymbol{u}}_s \, \mathrm{d}V. \tag{29}$$

This is a local measure and by using this for the evaluation of the total aerodynamic force we avoid the aforementioned issues. The numerically evaluated total aerodynamic force by the two different expressions has been found in agreement if the rate of change of vorticity due to diffusion and stretching is integrated in time by the explicit Euler method such that it is treated consistently with the penalization term.

3. Results

3.1. The impulsively started flow past a sphere at $\mathrm{Re} = 1000$

We simulate the impulsively started flow past a stationary sphere at $\mathrm{Re} = 1000$ as sketched in Fig. 1. The Reynolds number and dimensionless time, drag and lift coefficient are defined as respectively

$$\mathrm{Re} = \frac{UD}{\nu}, \quad t^* = \frac{tU}{D}, \quad C_D = \frac{F_x}{\left(\frac{1}{2}\rho U^2\right)\left(\frac{1}{4}\pi D^2\right)}, \quad C_L = \frac{F_y}{\left(\frac{1}{2}\rho U^2\right)\left(\frac{1}{4}\pi D^2\right)}, \tag{30}$$

where D is the diameter of the sphere. We use a grid spacing of $h = 128/D$ (unless otherwise stated). A second order explicit Runge–Kutta scheme is applied for the advancement of particles with time step size $\Delta t^* = 0.005$. This time step has

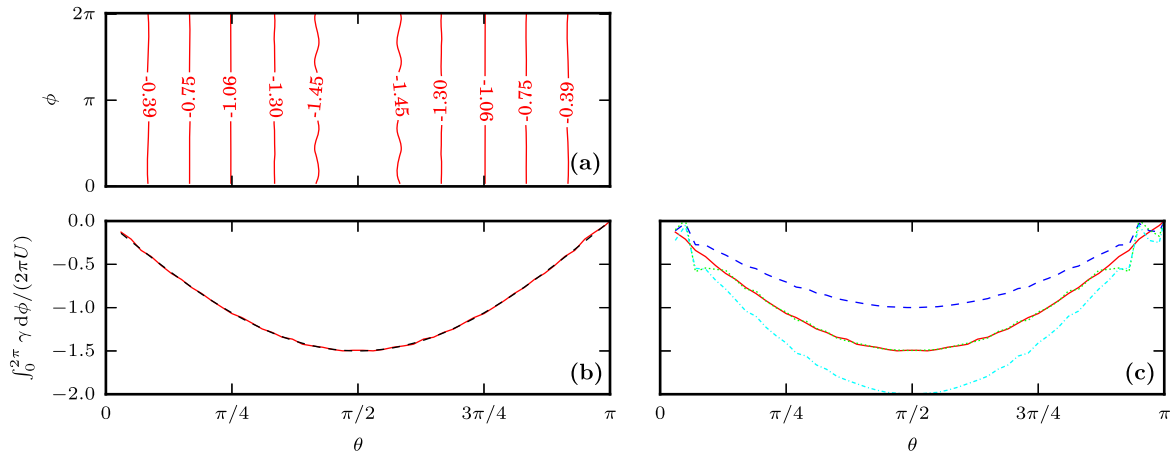

Fig. 2. The vortex sheet at $t^* = 0^+$ by the present 3D Brinkman penalization method. (a) Isocontours of vortex sheet strength (normalized by U) obtained with the iterative scheme as function of azimuthal angle, θ and polar angle ϕ. (b) The vortex sheet strength using the iterative scheme and averaged in the polar direction (——) compared to the exact potential solution (- - -). (c) Vortex sheet strength at $t^* = 0^+$ by the iterative scheme (——) and the non-iterative scheme using $\alpha = 1$ (- - -), $\alpha = \frac{3}{2}$ (·····) and $\alpha = 2$ (-·-·-).

been found to give accurate results and is identical to the time step used by Ploumhans et al. [14]. The extent of the domain is updated every 50th time step to prevent truncation of vortex particles that satisfy the threshold $|\boldsymbol{\omega}_p|/||\boldsymbol{\omega}_p||_\infty \geq 10^{-5}$. For the iterative scheme we employ a default convergence criteria of $\varepsilon = 0.05$.

3.1.1. The potential flow solution and the axisymmetric stream function

The potential flow past a sphere may be described as a singular distribution of vorticity at the surface of the sphere. The potential flow is axisymmetric. Hence, it has zero variation with the polar angle (ϕ) in a spherical coordinate system cf. Fig. 1. The vortex sheet is [32]

$$\gamma = -\frac{3}{2} U \sin\theta. \tag{31}$$

We compare the analytic solution (Eq. (31)) to our split-step result at the first time step of the impulsively started flow simulation. We refer to this as the solution at time $t^* = 0^+$. Though our simulation does not result in a singular distribution of vorticity at $t^* = 0^+$, we estimate the vortex sheet by interpolating the split-step vorticity onto a spherical grid ($N_r \times N_\theta \times N_\phi = 100 \times 50 \times 100$) and integrate in the radial direction as

$$\gamma = \int_0^\infty \omega_\phi^* \, \mathrm{d}r. \tag{32}$$

Fig. 2(a) and Fig. 2(b) shows that the iterative scheme using $\alpha = 1$ results in a sheet that is in excellent agreement with the potential flow solution. The obtained sheet is approximately constant in the polar direction and the variations may be explained by errors due to having sampled the geometry of the sphere on a Cartesian grid when discretizing the characteristic function of Eq. (2).

Fig. 2(c) shows the vortex sheet by the iterative scheme using $\alpha = 1$ compared to the vortex sheet by the non-iterative scheme for $\alpha = 1$, $\alpha = \frac{3}{2}$ and $\alpha = 2$. The initial vortex sheet produced in a single iteration using Eq. (21) is $\gamma(\theta) = -\alpha u_{\text{slip}}(\theta)$ when the solid is a sphere (in the absence of effects due to finite spatial resolution). The initial slip velocity is $u_{\text{slip}}(\theta) = U\sin(\theta)$, hence the potential solution is produced in a single iteration for $\alpha = \frac{3}{2}$. The figure shows that the non-iterative scheme produces an almost equally well matching solution using $\alpha = \frac{3}{2}$ as expected based on the aforementioned argument. Some oscillations are observed near $\theta = 0$ and $\theta = \pi$ due to finite spatial resolution. Evidently, the vortex sheet strength obtained without iterating is incorrect using other values of α

An axisymmetric stream function (φ) is computed from the simulated vector potential ($\boldsymbol{\psi}$), which is interpolated to a cylindrical grid ($N_r \times N_\phi \times N_x = 100 \times 100 \times 1.5D/h$) and averaged in the polar direction as

$$\varphi(r, x) = \frac{1}{2\pi} \int_0^{2\pi} r\boldsymbol{\psi}(r, \phi, x) \cdot \boldsymbol{e}_\phi \, \mathrm{d}\phi. \tag{33}$$

Isocontours of the axisymmetric stream function are shown in Fig. 3. The figure demonstrates that the iterative scheme is capable of accurately imposing the no-through boundary condition. The overestimation of the vortex sheet strength by

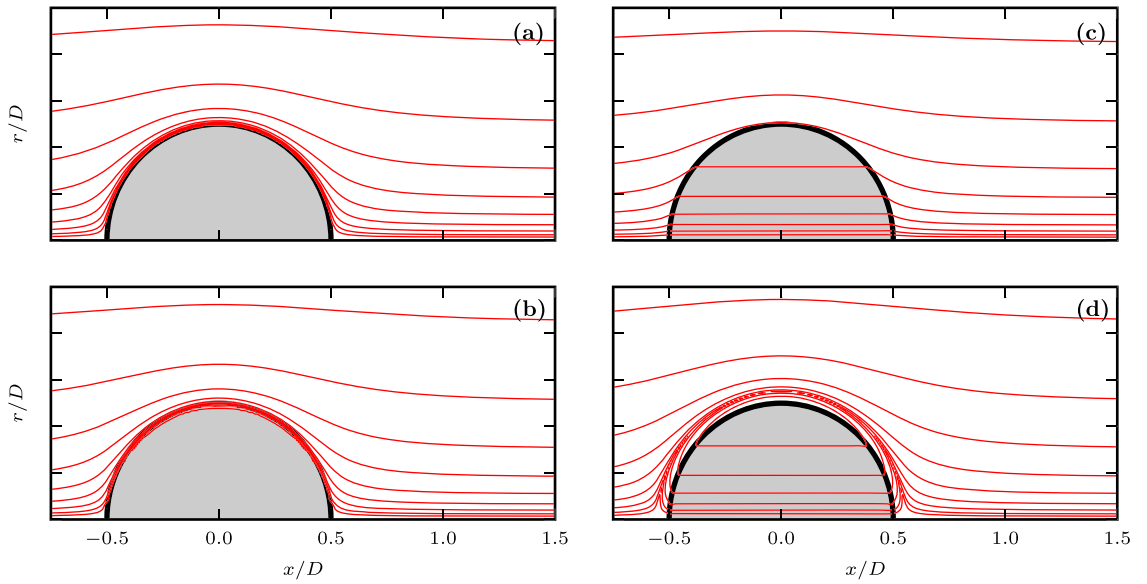

Fig. 3. Isocontours of axisymmetric stream function in 10 logarithmically spaced levels in the interval $[-1, 1]$ at $t^* = 0^+$. (a) Solution for the iterative scheme using $\alpha = 1$. (b) Solution for the non-iterative scheme using $\alpha = 1$. (c) Solution for the non-iterative scheme using $\alpha = \frac{3}{2}$. (d) Solution for the non-iterative scheme using $\alpha = 2$.

using $\alpha = 2$ with the non-iterative scheme causes a growth in the effective radius of the sphere and a back flow within the sphere at this time step. Setting $\alpha = \frac{3}{2}$ yields a better boundary condition as compared to the two other non-iterative cases shown but is not as smooth and accurate near the surface of the sphere as obtained with the iterative scheme.

3.1.2. Convergence of drag coefficient at the early times of the simulation

We now consider the time interval $t^* \in [0, 1]$ and verify the consistency of the proposed method by measuring the convergence of the relative error on the drag coefficient for various spatial resolutions against the best resolved case as

$$\text{error}(t^*) = \frac{|C_D(t^*) - C_{D\,\text{best resolved}}(t^*)|}{|C_{D\,\text{best resolved}}(t^*)|}. \tag{34}$$

The study is carried out for the iterative scheme using $\alpha = 1$ and mesh spacings $D/h = 16$, 32, 48, 64, 96, 128 and 256. The error is shown in Fig. 4 and the temporal variation of the drag coefficient in the case with resolution $D/h = 128$ is shown in Fig. 5(a). The decay of the error-norms is approximately second order cf. Fig. 4. The rate of convergence is not increased by applying a fourth order finite difference scheme for computation of Eq. (21) rather than a second order scheme. This observation is consistent with the dependency of the maximum order of accuracy that may be achieved when solving Poisson equation as Eq. (13), on the number of continuous derivative of the vorticity field. In the current method the vorticity field becomes singular as we compute the rate of change of vorticity as the derivative of a Heaviside function (χ). However, the resulting velocity field is ensured to be sufficiently smooth to be used to approximate the solution to the governing equations ($\boldsymbol{u} \in \mathcal{C}^2$). We do not find that it is necessary to introduce an ad hoc mollification of χ. Instead we explicitly regularize the vorticity field by which the observed rate of convergence of the current method correspondents to that reported using a mollified χ [8]. The same study was also carried out using the M_6^* interpolation kernel. The results showed an insignificant improvement on the error level and the same rate of convergence as reported for M_4'. We relate this to the explicit regularization that effectively removes singularities at the solid interface before interpolation each time step.

3.1.3. Comparison of iterative and non-iterative scheme at early times

We compare the drag coefficient obtained using the iterative and the non-iterative scheme using $\alpha = 1$ in Fig. 5(a). For the impulsively started flow past a sphere at the current Reynolds number there is no visible deviation between the two in the considered time interval.

The velocity residual at the end of the penalization step, for the iterative and the non-iterative scheme, is shown in Fig. 5(b). The L_2-norm of the residual obtained using the iterative scheme, requiring on average 30 iterations per time step to fulfill the convergence criteria, is approximately one order of magnitude lower than the norm obtained by the non-iterative scheme. This indicates that the iterative scheme enforces the solid boundary condition one order of magnitude more accurately than the non-iterative scheme. This is essentially the same as observed in 2D for the impulsively started flow past a cylinder at $\text{Re} = 9500$ by Hejlesen et al. [7].

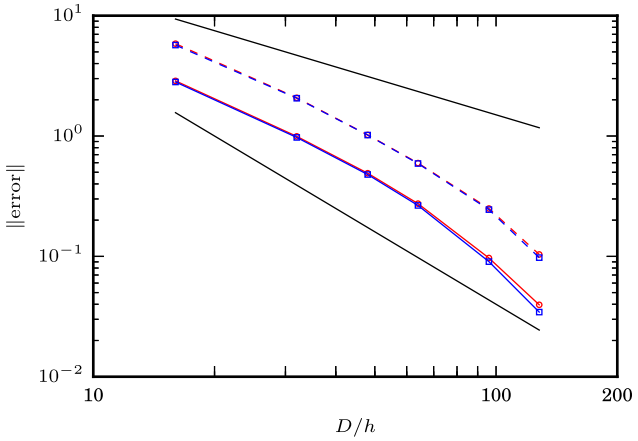

Fig. 4. Convergence of the relative error on the drag coefficient for the impulsively started flow past a sphere at Re = 1000 using the 3D iterative Brinkman method and a fixed time step of $\Delta t^* = 0.005$. The relative error is measured by comparing with the solution obtained using a spatial resolution of $h = D/128$ in the time interval $t^* \in [0, 5]$. L_∞-norm (—○—) and L_2-norm (- ○ -) using a second order approximation to Eq. (21). L_∞-norm (—□—) and L_2-norm (- □ -) using a fourth order approximation to Eq. (21). Indication of respectively $\mathcal{O}(h^1)$ and $\mathcal{O}(h^2)$ convergence (——).

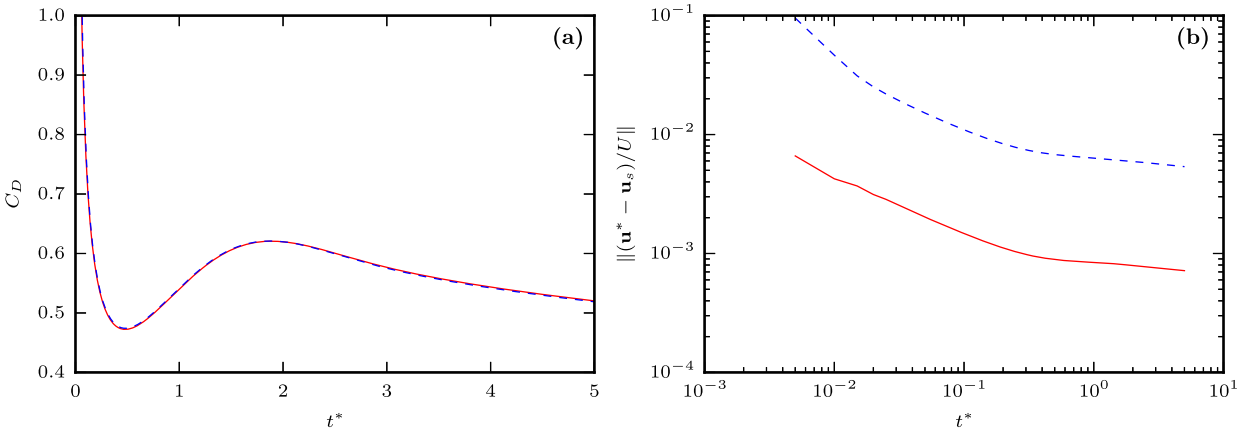

Fig. 5. Impulsively started flow past a sphere at Re = 1000 simulated using $h = D/128$ and $\Delta t^* = 0.005$. (a) Time variation of the drag coefficient for the iterative scheme (——) and the non-iterative scheme (- - -). (b) Time variation of the L_2-norm of the velocity residual for the iterative scheme (——) and the non-iterative scheme (- - -).

The rate at which the residual velocity within the solid at various time steps decays with the iteration number (N_i) has been plotted in Fig. 6. The variation has been measured for up to 1000 iterations at each of these time steps, hence exceeding the number of iterations needed to fulfill the aforementioned termination criteria. In this case, the asymptotic rate is close to −0.5 depending on which time step and norm is considered. The additional cost of iterating the penalization vorticity relative to the cost of not iterating has been measured to be about 260% at time $t^* = 0$. At this time the penalization subdomain constitutes about 40% of the full domain. At time $t^* = 5.0$ the domain has expanded to encapsulate all vorticity with strength above the given threshold and consequently the penalization subdomain constitutes about 10%. This reduces the relative additional cost of iterating to about 120%. This indicates that for simulations with extensive wakes, where the penalization subdomain may be small compared to the full domain, it is cheaper to reduce the velocity residual of the penalization by performing iterations rather than by reducing the global time step of the simulation.

3.1.4. *Qualitative comparison of perturbed flow at later stages*

Following Ploumhans et al. [14] and Mimeau et al. [13], we calculate the variation in time of the drag and lift coefficient in the interval $t^* \in [0, 20]$ having applied a perturbation to the free-stream velocity that breaks the axisymmetry

$$U_y = \begin{cases} 0.1 \sin(\pi (t^* - 3)) & \text{if } 3 < t^* < 4 \\ 0 & \text{else.} \end{cases} \tag{35}$$

Due to the perturbation a vortical structure is shed in the near wake from $t^* = 10$–14 forming a complex 3D wake. This shedding causes significant variations in the force coefficients as shown in Fig. 7(a). The force coefficients are found in good qualitative agreement with the results of Ploumhans et al. [14] and Mimeau et al. [13] cf. Fig. 7(a). In the current simulation,

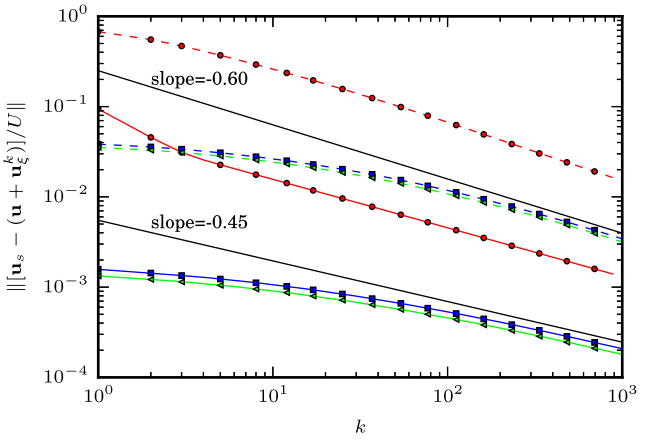

Fig. 6. Impulsively started flow past a sphere at $\mathrm{Re} = 1000$ simulated using $h = D/128$ and $\Delta t^* = 0.005$. Decay of L_2-norm (solid lines) and L_∞-norm (dashed lines) of the velocity residual within the solid body as function of the iteration number (N_i) tested at time step 1 ($t^* = 0$) (—○—), 200 ($t^* = 1.0$) (—□—) and 1000 ($t^* = 5.0$) (—◁—).

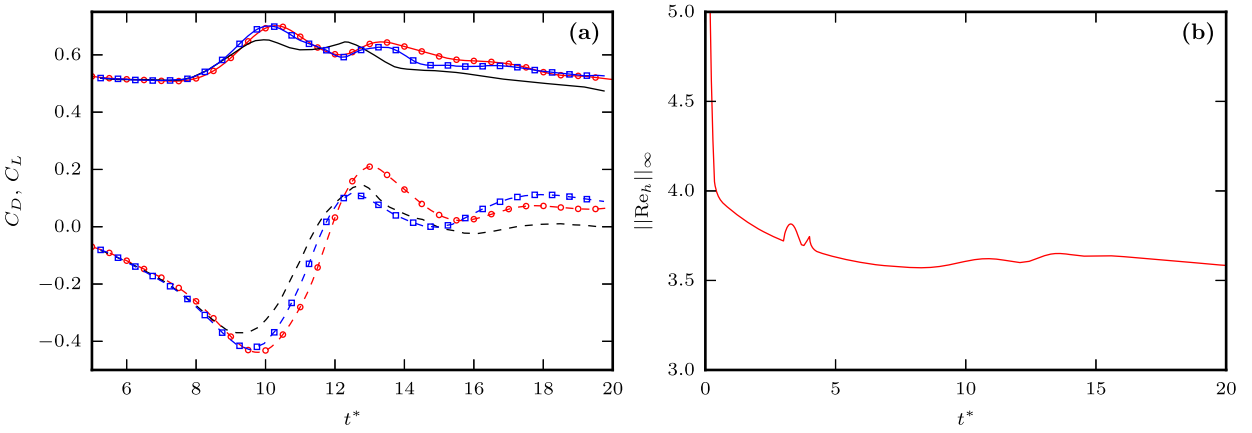

Fig. 7. Time variation of simulations diagnostics in the impulsively started and perturbed flow past a sphere at $\mathrm{Re} = 1000$. (a) Drag coefficient (—○—) and lift coefficient (- ⊖ -) from present study. Drag coefficient (——) and lift coefficient (- - -) from Ploumhans et al. [14]. Drag coefficient (—□—) and lift coefficient (- ⊟ -) from Mimeau et al. [13]. (b) Time variation of the maximum mesh Reynolds number.

the magnitudes of the obtained coefficients are slightly higher and the two extrema of the drag coefficient time history at $t^* \simeq 10.3$ and 13.3 are delayed as compared to Ploumhans et al. [14], which is the same tendency seen in the results by Mimeau et al. [13]. The vortical structures of the flow, identified by the λ_2-criteria [33], at various times are shown in Fig. 8.

Ploumhans et al. [14] further reported the maximum mesh Reynolds number,

$$\mathrm{Re}_{h\,\max} = \| \frac{|\boldsymbol{\omega}|h^2}{\nu} \|_\infty \tag{36}$$

as a diagnostic of the effective flow resolution in their simulation. The mesh Reynolds number in the present simulation is shown in Fig. 7(b). The figure shows that in present study the maximum Reynolds number is at its maximum close to $t^* = 0$ due to the singularity occurring in the impulsively started flow. It rapidly decays to a value below 4 as the flow develops. Ploumhans et al. [14] reported a maximum mesh Reynolds number increasing from approximately 4 to 15–20 in their entire domain but approximately 3 in the boundary layer. The later is close to the present result since the grid resolution near the solid body is about the same. It is reasonable to believe that the wake is better resolved in the present simulation as consequence of the uniform resolution. Ploumhans et al. [14] used a reduced resolution in the far wake for computational efficiency.

The vortical structures observed at $t^* = 20$ in the present study shown in Fig. 8 appear more entangled than those reported by Ploumhans et al. [14]. This may be due to a suppression of instabilities in the shed structure caused by the presumed coarser spatial resolution of the wake in that study.

The number of particles simulated increase from $\simeq 2 \times 10^6$ to $\simeq 7 \times 10^7$ in the current simulation, which is significantly more than the $\simeq 4.6 \times 10^5$ to $\simeq 2.3 \times 10^6$ particles that were used in the simulation by Ploumhans et al. [14]. The present simulation requires approximately 100 hours on 256 cores of the Intel Xeon E5640 processors.

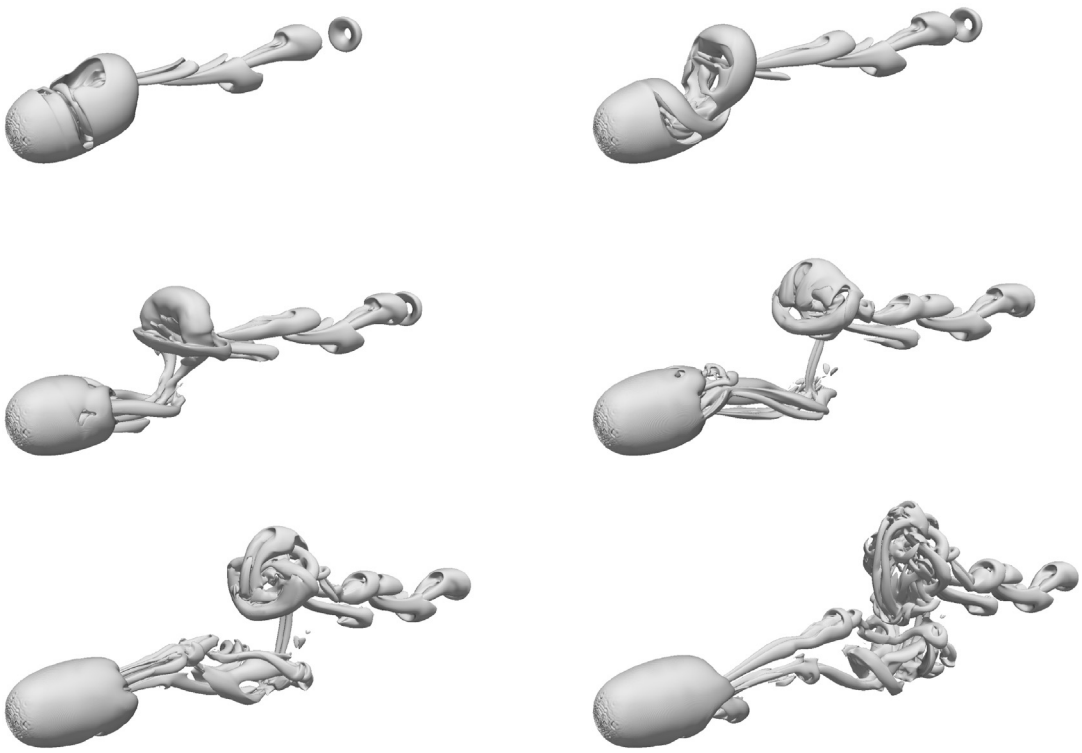

Fig. 8. Visualization of vortical structures of the impulsively started and perturbed flow past a sphere at $\mathrm{Re} = 1000$. Isosurface of $\lambda_2 = -10^{-5}$ at $t^* = 10, 12, 14, 16, 18, 20$ (left to right, top to bottom).

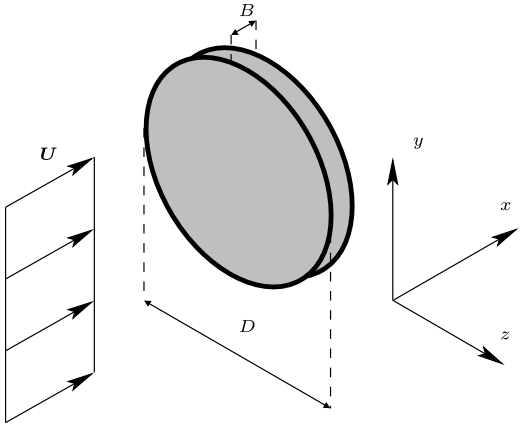

Fig. 9. Impulsively started flow ($\boldsymbol{U}$) past a circular disc of finite thickness (B) and diameter (D). The origin of the Cartesian coordinate system is in the sketch displaced from its actual origin being at the center of the disc.

3.2. *Impulsively started flow normal to a disc at* $\mathrm{Re} = 500$

The impulsively started flow normal to a circular disc at $\mathrm{Re} = 500$ is considered next. The setup is sketched in Fig. 9. The Reynolds number and non-dimensionless time, drag force we define respectively as

$$\mathrm{Re} = \frac{UD}{\nu}, \quad t^* = \frac{tU}{D}, \quad C_D = \frac{F_x}{\frac{1}{2}\rho U^2 D^2}, \tag{37}$$

where D is the diameter of the disc. The thickness of the disk is $B = D/16$. Again the second order explicit Runge–Kutta scheme is applied for the advancement of particles and the extent of the domain is updated as in the sphere simulation. Simulations were performed for spatial resolution $h = D/128$ and $h = D/256$ corresponding to a disc thickness of 8 cells and 16 cells respectively.

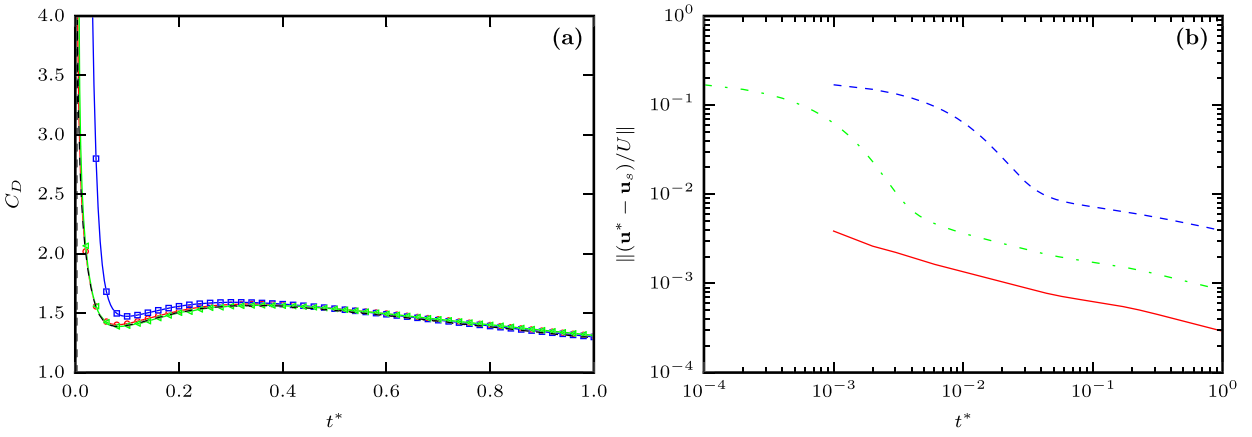

Fig. 10. Impulsively started flow normal to disc at Re = 500. (a) Drag coefficient obtained for the iterative scheme using $\Delta t^* = 0.001$ (—○—). Drag coefficient obtained for the non-iterative scheme using $\Delta t^* = 0.001$ (—□—) and $\Delta t^* = 0.0001$ (—◁—). Reference solution from a high resolution, axisymmetric simulation performed using a commercial finite-volume code (- - -). (b) Time variation of the L_2-norm of the velocity residual. Iterative scheme using $\Delta t^* = 0.001$ (—○—), non-iterative scheme using $\Delta t^* = 0.001$ (—□—) and $\Delta t^* = 0.0001$ (—◁—).

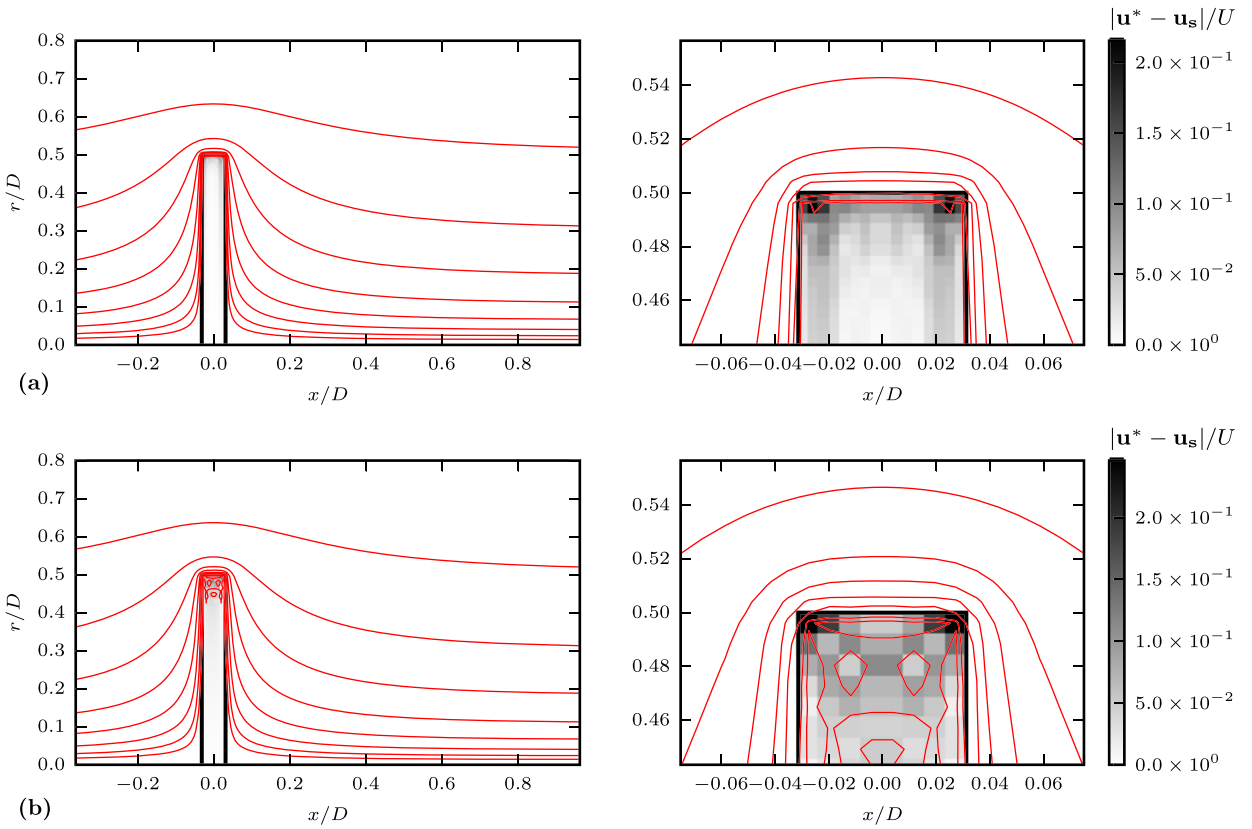

Fig. 11. Impulsively started flow normal to disc at Re = 500 at $t^* = 0^+$. Isocontours of the stream function in 10 logarithmically spaced levels in the interval $[-1, 1]$ (——) and indication of velocity residual within disc averaged in polar direction (grayscale). Zoom of the disc tip shows the maximum velocity residual is localized at the upstream edge, where streamlines may be seen to cross the interface. (a) Solution for spatial resolution $h = D/128$. (b) Solution for spatial resolution $h = D/256$.

3.2.1. Comparison of iterative and non-iterative scheme

The drag coefficient obtained for the disc flow is, unlike the sphere flow, significantly affected by the choice of penalization scheme. The drag coefficients obtained from the iterative and the non-iterative scheme using $\alpha = 1$ and $h = D/256$ are compared in Fig. 10(a). The figure shows that the iterative scheme match the reference well, when using a time step of

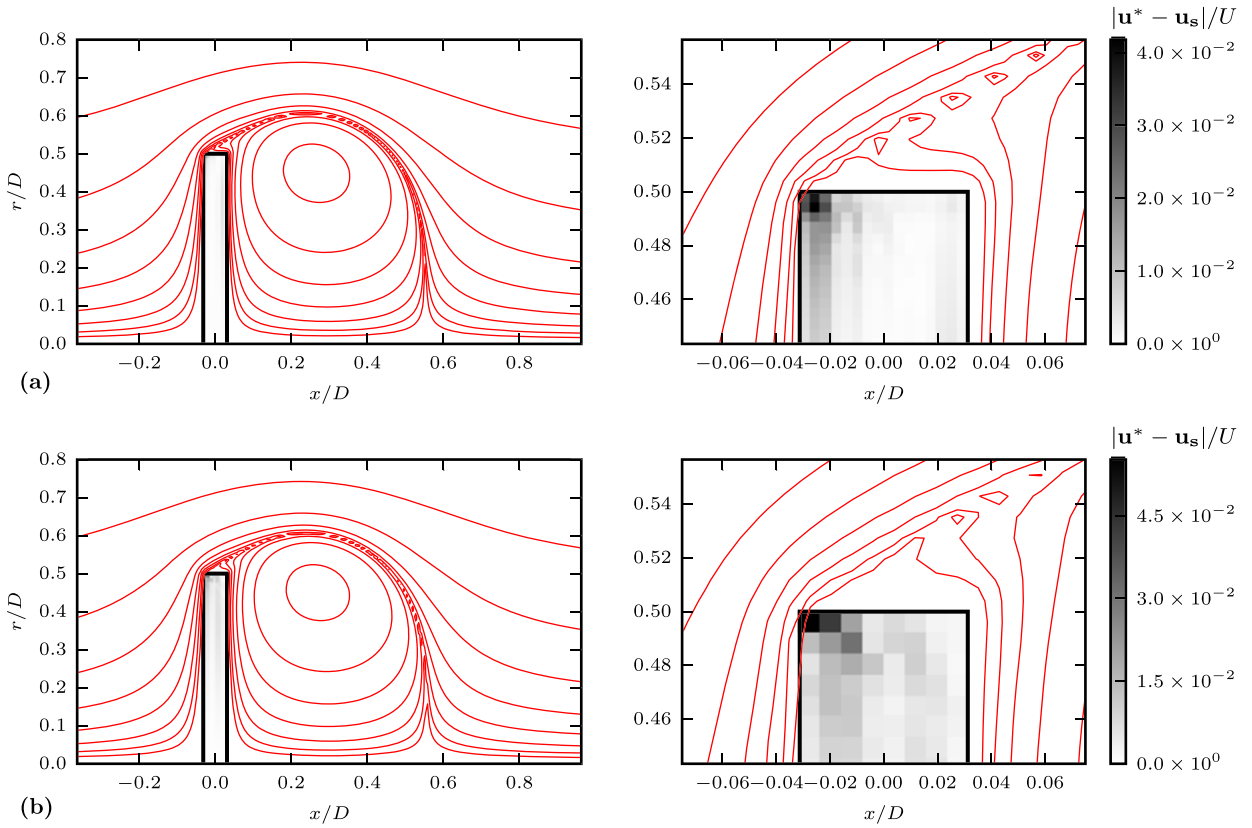

Fig. 12. Impulsively started flow normal to disc at $\mathrm{Re} = 500$ at $t^* = 1$. Isocontours of the stream function in 10 logarithmically spaced levels in the interval $[-1, 1]$ (——) and indication of velocity residual within disc averaged in polar direction (grayscale). Zoom of the disc tip shows the maximum velocity residual is localized at the upstream edge, where streamlines may be seen to cross the interface. (a) Solution for spatial resolution $h = D/128$. (b) Solution for spatial resolution $h = D/256$.

$\Delta t^* = 0.001$. Using the same time step the non-iterative scheme significantly overestimates the drag coefficient for $t^* < 0.2$, since this scheme requires several time steps to impose the boundary conditions accurately on the surface of the disc. This scheme requires a time step of $\Delta t^* = 0.0001$ to match the reference solution.

As in the simulation of the flow past the sphere, the iterative method impose a visibly accurate boundary condition from the first time step depending on the spatial resolution. This may be seen from the isocontours of the axisymmetric stream function shown in Fig. 11. It was observed that results obtained for $h = D/256$ complied better with the reference results as compared to $h = D/128$ independent of global time step and penalization scheme. We relate this to the additional degrees of freedom within disc where the penalization vorticity may be non-zero and to the reduced smoothing of the boundary at the higher resolution.

In this case the maximum residual velocity for the non-iterative scheme is $\mathcal{O}(1)$ until $t^* = 0.1$–0.5 (not shown) whereas it is lower but still significant ($\mathcal{O}(0.1)$) for the iterative scheme (cf. Fig. 11) using the criteria $\varepsilon = 0.05$ which require approximately 30 iterations per time step for both spatial resolutions.

However it is noted that the L_2-norm of the residual for the iterative scheme is at any time less than 0.004 which is not the case for the non-iterative scheme until after approximately 1000 time steps at $t^* = 1$ when using a time-step of $\Delta t^* = 0.001$ as shown in Fig. 10(b).

It is observed that the maximum residual in the iterative scheme is located at the edges of the disc, where we see streamlines cross the solid boundary. The regularization applied when solving the Poisson equation ensures a smooth velocity field across the boundary, hence the edges of the solid are effectively rounded and one may expect a velocity residual here larger than elsewhere in the solid at any time. This area near the edge may be reduced by increasing the spatial resolution as may be seen in Fig. 12, which shows the isocontours of the axisymmetric stream function and the averaged velocity residual within the solid at time $t^* = 1.0$ for grid sizes $h = D/128$ and $h = D/256$.

Fig. 13 shows the rate at which the residual velocity within the solid decays with the iteration number (k). As for the impulsively started flow past the sphere, the asymptotic rate is around -0.5. The rate is steeper the first few iterations of the first time step because of the geometry in this case. So indeed it is possible to reduce the velocity level even further by increasing the number of iterations, but the rate at which the residual decays is slow.

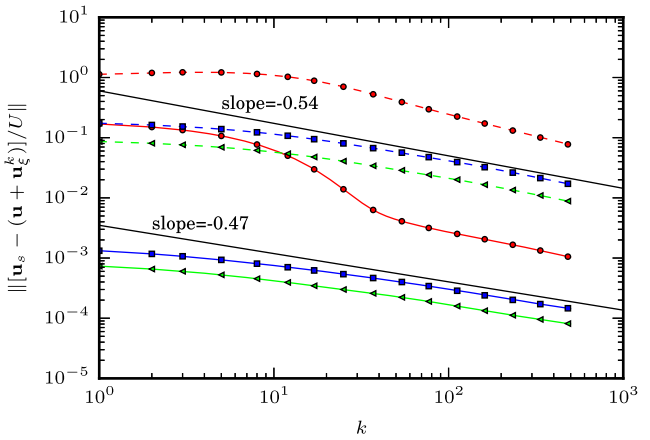

Fig. 13. Impulsively started flow normal to a disc at $\mathrm{Re} = 500$ simulated using $h = D/256$ and $\Delta t^* = 0.001$. Decay of L_2-norm (solid lines) and L_∞-norm (dashed lines) of the velocity residual within the solid body as function of the iteration number (k) tested at time step 1 ($t^* = 0$) (—○—), 200 ($t^* = 0.2$) (—□—) and 1000 ($t^* = 1.0$) (—◁—).

4. Conclusions

The present work has presented a 3D iterative Brinkman method for accurate simulation of unsteady flows. The work is based on the 2D method proposed by Hejlesen et al. [7].

The method has been validated for the impulsively started flow past a sphere at $\mathrm{Re} = 1000$. The iterative scheme produces a vortex sheet at the first time-step of the simulation ($t^* = 0^+$) that agrees with the exact potential flow solution. At later stages the unsteady force coefficients obtained have been found to be comparable to results obtained by Ploumhans et al. [14] and Mimeau et al. [13] using a boundary element method in a vortex particle method and vortex penalization method respectively.

The impulsively started flow normal to a circular disc of finite thickness at $\mathrm{Re} = 500$ has also been considered and found to be a challenging problem for the Brinkman penalization method due to the geometry having the majority of its surface area orientated normal to the free-stream. This introduces a delay in the enforcement of the solid boundary condition for the non-iterative scheme. This is a consequence of the lack of global coupling otherwise imposed by the elliptic kinematic relation between vorticity and velocity. The iterative Brinkman method accounts for this and has been found to produce a time variation of the simulated drag coefficient in agreement with a reference solution using a time step that is five to ten times larger than what is required with the corresponding non-iterative scheme.

We note that at times away from the impulsive start the iterative and non-iterative solutions are comparable in the presented cases, thus the benefit of the iterative process on the solution is negligible at these time stages. Future work includes the study of continuously accelerated and deforming solids which may reveal the full potential of the iterative process in 3D.

Acknowledgements

The research was funded by the Danish Council for Independent Research grant no. 4184-00349B. We would like to acknowledge the helpful discussion with Petros Koumoutsakos, Anthony Leonard and Johannes Tophøj Rasmussen.

References

[1] C. Peskin, Flow patterns around heart valves: a numerical study, J. Comput. Phys. 10 (1972) 252–271.
[2] D. Goldstein, R. Handler, L. Sirovich, Modeling a no-slip flow boundary with an external force field, J. Comput. Phys. 105 (1993) 354–366.
[3] P. Angot, C.-H. Bruneau, P. Fabrie, A penalization method to take into account obstacles in incompressible viscous flows, Numer. Math. 81 (1999) 497–520.
[4] K. Khadra, P. Angot, S. Parneix, J.P. Caltagirone, Fictitious domain approach for numerical modelling of Navier–Stokes equations, Int. J. Numer. Methods Fluids 34 (2000) 651–684.
[5] N.K.-R. Kevlahan, J.-M. Ghidaglia, Computation of turbulent flow past an array of cylinders using a spectral method with Brinkman penalization, Eur. J. Mech. B, Fluids 20 (2001) 333–350.
[6] J.T. Rasmussen, M.M. Hejlesen, A. Larsen, J.H. Walther, Discrete vortex method simulations of the aerodynamic admittance in bridge aerodynamics, J. Wind Eng. Ind. Aerodyn. 98 (2010) 754–766.
[7] M.M. Hejlesen, P. Koumoutsakos, A. Leonard, J.H. Walther, Iterative Brinkman penalization for remeshed vortex methods, J. Comput. Phys. 280 (2015) 547–562.
[8] M. Gazzola, P. Chatelain, W.M. van Rees, P. Koumoutsakos, Simulations of single and multiple swimmers with non-divergence free deforming geometries, J. Comput. Phys. 230 (2011) 7093–7114.
[9] M. Coquerelle, G.-H. Cottet, A vortex level set method for the two-way coupling of an incompressible fluid with colliding rigid bodies, J. Comput. Phys. 227 (21) (2008) 9121–9137.

[10] D. Rossinelli, M. Bergdorf, G.-H. Cottet, P. Koumoutsakos, GPU accelerated simulations of bluff body flows using vortex particle methods, J. Comput. Phys. 229 (89) (2010) 3316–3333.
[11] M. El Ossmani, P. Poncet, Efficiency of multiscale hybrid grid-particle vortex methods, Multiscale Model. Simul. 8 (5) (2010) 1671–1690.
[12] C. Mimeau, F. Gallizio, G.H. Cottet, I. Mortazavi, Vortex penalization method for bluff body flows, Int. J. Numer. Methods Fluids 79 (2) (2015) 55–83.
[13] C. Mimeau, G.H. Cottet, I. Mortazavi, Direct numerical simulations of three-dimensional flows past obstacles with a vortex penalization method, Comput. Fluids 136 (2016) 331–347.
[14] P. Ploumhans, G.S. Winckelmans, J.K. Salmon, A. Leonard, M.S. Warren, Vortex methods for direct numerical simulation of three-dimensional bluff body flows: applications to the sphere at $Re = 300$, 500 and 1000, J. Comput. Phys. 178 (2002) 427–463.
[15] J.J. Monaghan, Extrapolating B splines for interpolation, J. Comput. Phys. 60 (2) (1985) 253–262.
[16] M. Bergdorf, P. Koumoutsakos, A Lagrangian particle-wavelet method, Multiscale Model. Simul. 5 (3) (2006) 980–995.
[17] W.M. van Rees, A. Leonard, D.I. Pullin, P. Koumoutsakos, A comparison of vortex and pseudo-spectral methods for the simulation of periodic vortical flows at high Reynolds numbers, J. Comput. Phys. 230 (2011) 2794–2805.
[18] M.M. Hejlesen, J.T. Rasmussen, P. Chatelain, J.H. Walther, A high order solver for the unbounded Poisson equation, J. Comput. Phys. 252 (2013) 458–467.
[19] M.M. Hejlesen, T. Rasmussen Johannes, P. Chatelain, J.H. Walther, High order Poisson solver for unbounded flows, Proc. IUTAM 18 (2015) 56–65.
[20] M.M. Hejlesen, A High Order Regularisation Method for Solving the Poisson Equation and Selected Applications using Vortex Methods, PhD thesis, Technical University of Denmark, February 2016.
[21] R.W. Hockney, J.W. Eastwood, Computer Simulation Using Particles, 2nd edition, Institute of Physics Publishing, Bristol, PA, USA, 1988.
[22] R.W. Hockney, The potential calculation and some applications, Methods Comput. Phys. 9 (1970) 136–210.
[23] J.W. Eastwood, D.R.K. Brownrigg, Remarks on the solution of Poisson's equation for isolated systems, J. Comput. Phys. 32 (1979) 24–38.
[24] P. Koumoutsakos, A. Leonard, High-resolution simulation of the flow around an impulsively started cylinder using vortex methods, J. Fluid Mech. 296 (1995) 1–38.
[25] P. Koumoutsakos, Inviscid axisymmetrization of an elliptical vortex ring, J. Comput. Phys. 138 (1997) 821–857.
[26] P. Chatelain, A. Curioni, M. Bergdorf, D. Rossinelli, W. Andreoni, P. Koumoutsakos, Billion vortex particle direct numerical simulations of aircraft wakes, Comput. Methods Appl. Mech. Eng. 197 (2008) 1296–1304.
[27] J.T. Rasmussen, G.-H. Cottet, J.H. Walther, A multiresolution remeshed vortex-in-cell algorithm using patches, J. Comput. Phys. 230 (17) (2011) 6742–6755.
[28] J.C. Wu, A Theory for Aerodynamic Forces and Moments, Technical report, Georgia Institute of Technology, September 1978.
[29] F. Noca, D. Shiels, D. Jeon, Measuring instantaneous fluid dynamic forces on bodies, using only velocity fields and their derivatives, J. Fluids Struct. 11 (1997) 345–350, special brief note.
[30] F. Noca, D. Shiels, D. Jeon, A comparison of methods for evaluating time-dependent fluid dynamic forces on bodies using only velocity fields and their derivatives, J. Fluids Struct. 13 (1999) 551–578.
[31] P.G. Saffman, Vortex Dynamics, Cambridge University Press, 1992.
[32] G.K. Batchelor, An Introduction To Fluid Dynamics, 1st edition, Cambridge University Press, 1967.
[33] J. Jeong, F. Hussain, On the identification of a vortex, J. Fluid Mech. 285 (1995) 69–94.